https://doi.org/10.5194/egusphere-2026-2451
Preprint. Discussion started: 8 May 2026

Greenland mass change using range acceleration from GRACE-FO

Barbara Jenny[1], Tim Jensen[1], and René Forsberg[1]
[1]DTU Space, Elektrovej 327, 2800 Kgs. Lyngby, Danmark
Correspondence: Barbara Jenny (barbj@space.dtu.dk)

Abstract. Observations of ice mass change with GRACE and GRACE-FO are limited in both temporal and spatial resolution. For the Greenland ice sheet, standard processing can resolve monthly mass change at the scale of large drainage basins, not at the level of individual glaciers or smaller regions. For GRACE-FO, a method using the range acceleration measurements to calculate instantaneous line-of-sight gravity has been used to study hydrological extremes such as floods and storm surges. In this paper, we look at the Greenland ice sheet and use the line-of-sight gravity signal to estimate 5-day mass change for four summers. We also include altimetry data to try to improve the spatial resolution of the observed mass change. The amplitude of the estimated mass change is within the range of monthly mass change estimates. The choice of regularisation clearly affects the spatial distribution, which in turn affects estimates at basin scales or even at smaller scales. Additionally, the noise level increases relative to the monthly signal, and the regularisation based on altimetry data increases the correlation among mass points compared to Tikhonov regularisation. Estimating mass change based on line-of-sight gravity is possible, although the spatial distribution remains sensitive to the choice of regularisation. Nonetheless, the approach shows promise for resolving short-term mass-change events and motivates further refinement of line-of-sight gravity-based inversion techniques for future satellite gravimetry missions.

1 Introduction

The Gravity Recovery and Climate Experiment (GRACE) and its Follow-On (GRACE-FO) missions have proven valuable for monitoring the state of the Greenland ice sheet by revealing seasonal mass changes and decadal mass-loss trends. While daily GRACE solutions are available from Mayer-Gürr et al. (2018); Kvas et al. (2019), they have limited spatial resolution and require stabilisation using de-aliasing models (Kurtenbach et al., 2012). In this paper, we consider a different approach based on line-of-sight gravity observations and inversion to point mass changes on the surface of the Earth. To observe ice mass change at sub-monthly timescales and at a spatial resolution comparable to monthly ice mass change products, we use range-acceleration observations from the Laser Ranging Interferometer (LRI) instrument on board GRACE-FO and combine them with altimetry data to constrain the spatial distribution of the estimated mass change.

Previous research has repeatedly shown that, using dynamic orbits and LRI data, one can compute residual line-of-sight gravity signals, commonly referred to as line-of-sight gravity differences (LGD) (Ghobadi-Far et al., 2018, 2022). This method was primarily used to study hydrological signals such as storm surges or heavy rainfall. Li et al. (2024) studied sub-monthly mass changes in Western Europe and Central China by inverting the LGD using a point-mass approach. In their later study, Li et al. (2025) discussed daily total water storage change based on the inversion of LGD using Slepian and B-spline functions. The higher temporal resolution of the approach is also investigated by Khaki et al. (2023), who successfully assimilated LGD into land surface models.

Using a similar approach, we invert residual line-of-sight gravity over Greenland and incorporate height-change trends to regularise the spatial distribution of mass change. Applying this method for the first time in Greenland, while integrating altimetry data in the inversion, we derive mass changes at 5-day intervals during four summer periods. First, we compare the results for all of Greenland with other solutions. Second, we use the Ilulissat glacier as a case study to examine if this method can properly resolve this smaller area and how the altimetry-based regularisation affects the spatial distribution of the estimated mass change. These first results are promising but also indicate that further calibration of the method is needed for small-scale mass-change features, such as ice mass change.

2 Materials and methods

The laser ranging instrument (LRI) was an experimental instrument aboard GRACE-FO that collected inter-satellite ranging data until July 2023. Since then, LRI has been running in diagnostic mode to reduce thruster activation and overall fuel usage (Landerer et al., 2023). There are also several data gaps, including July and August 2022. To estimate mass change from the observed GRACE-FO laser intersatellite range accelerations, we need:

- reference range accelerations from estimated orbits (Mayer-Gürr et al., 2021) to get residual range accelerations,
- a filter to reduce residual range accelerations to line-of-sight gravity differences (LGD) (Ghobadi-Far et al., 2018),
- LGD from monthly Level 2 gravity fields (Mayer-Gürr et al., 2018; Ince et al., 2019),
- a GIA correction (Caron et al., 2018), and
- a regularisation scheme tailored to the study area.

2.1 GRACE-FO data and orbit estimation

In this paper, reference range accelerations are generated based on orbits estimated using the GROOPS software package (Mayer-Gürr et al., 2021). Table 1 shows the GRACE-FO Level 1B Data and the models used in the orbit estimation. Similar to Ghobadi-Far et al. (2018), orbits are estimated based on static gravity field components and tidal signals. As a result, the LGD represents residuals in the gravity field with respect to the chosen static field (nominal epoch 1 January 2010) and background models.

Figure 1 shows the observation and the model areas used for the inversion. The model area for Greenland is based on the Greenland Mass Balance (GMB) grid of the extended ESA CCI product by Barletta et al. (2020). The model area for Iceland and Ellesmere Island in northern Canada was generated by spacing mass points roughly 45 km apart. The observation time is

https://doi.org/10.5194/egusphere-2026-2451
Preprint. Discussion started: 8 May 2026

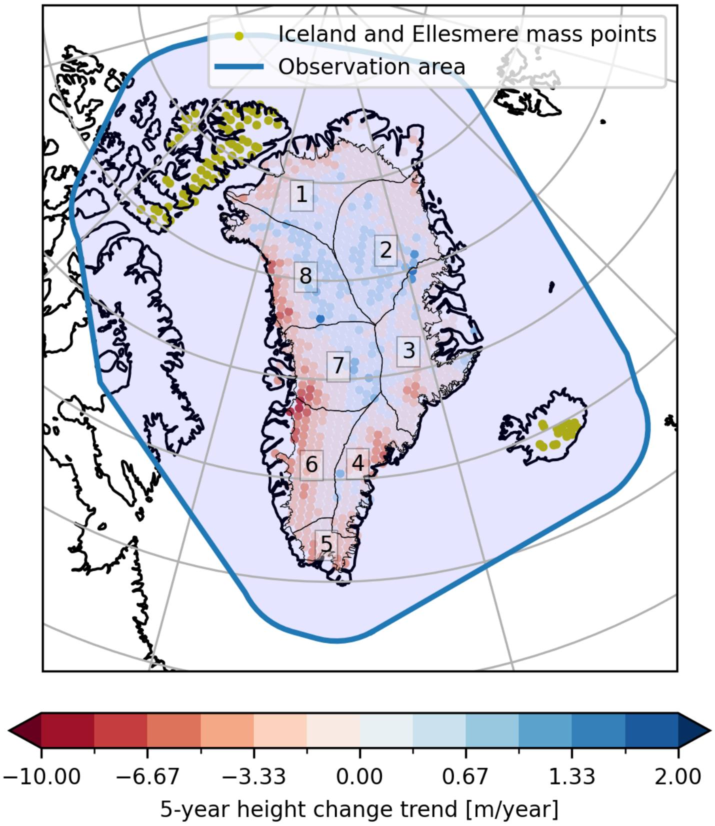

Figure 1. The model area for the inversion is represented by points in Greenland, Iceland and Ellesmere Island. The colours represent the ice height change trend during the 5-year period from 2010–2015, derived by downsampling the extended ESA CCI height trends by Simonsen and Sørensen (2020) for Greenland to the ESA CCI GMB grid by Barletta et al. (2020). Note the asymmetrical colour bar. For Iceland and Ellesmere Island, no height trends are used, and they are treated differently in the inversion. The blue area marks the observation area, defined to be at least 400 km larger in every direction than the model area when projected to the ground. The lines and numbers mark the Greenland Zwally basins (Zwally et al., 2012).

Table 1. Models and data used in orbit estimation with GROOPS

Description	Data or Model	Source
Data		
initial orbit	GNV1B	NASA Jet Propulsion Laboratory (JPL) (2019)
satellite attitude	SCA1B	NASA Jet Propulsion Laboratory (JPL) (2019)
intersatellite ranging	KBR1B	NASA Jet Propulsion Laboratory (JPL) (2019)
non-gravitational forces	ACT1B and THR1B	NASA Jet Propulsion Laboratory (JPL) (2019)
Potential Models		
atmosphere and ocean de-aliasing	AOD1B RL07	Shihora et al. (2022)
static gravity field	GOCO06s (d/o 0-300)	Kvas et al. (2021)
solid earth tides	IERS 2010	Gérard and Luzum (2010)
ocean tides	FES2014b	Lyard et al. (2021)
atmospheric tides	TiME22	Sulzbach et al. (2022)
pole tides	Mean Pole	Gérard and Luzum (2010)
ocean pole tides	Desai 2004	Desai (2002)
Other		
earth rotation	IAU2000	Gérard and Luzum (2010)
ephemerides	JPL DE432	Folkner et al. (2014)
relativistic corrections	IERS 2010	Gérard and Luzum (2010)

five days per set, covering June, July, and August for the years 2019, 2020, 2021, and June in 2022. These months were chosen as we expect most of the mass loss to occur during summer.

2.2 Estimating line-of-sight gravity from range acceleration

The line-of-sight (LOS) gravity, g_{12}^{LOS}, is related to range accelerations $\ddot{\rho}$ as described in Ghobadi-Far et al. (2018).

$$\ddot{\rho} = \frac{\mathrm{d}}{\mathrm{d}t}\dot{\rho} = \frac{\mathrm{d}}{\mathrm{d}t}(\dot{\mathbf{r}}_{12}\cdot\mathbf{e}_{12}) = \ddot{\mathbf{r}}_{12}\cdot\mathbf{e}_{12} + \dot{\mathbf{r}}_{12}\cdot\dot{\mathbf{e}}_{12} \tag{1}$$

$$= g_{12}^{LOS} + \frac{1}{\rho}\left(|\dot{\mathbf{r}}_{12}|^2 - \dot{\rho}^2\right) , \tag{2}$$

with range $\rho = |\mathbf{r}_{12}|$, range rate $\dot{\rho} = \dot{\mathbf{r}}_{12}\cdot\mathbf{e}_{12}$, relative velocity $\dot{\mathbf{r}}_{12}$ and LOS vector $\mathbf{e}_{12} = \mathbf{r}_{12}/\rho$. The relative position vector $\mathbf{r}_{12} = \mathbf{r}_2 - \mathbf{r}_1$ is derived from the satellite positions. The LGD, $\delta g_{12}^{\mathrm{LOS}}$, is the difference between LOS gravity computed from Eq. (1) and LOS gravity from estimated orbits

$$\delta g_{12}^{\mathrm{LOS}} = g_{12}^{\mathrm{LOS}} - g_{12}^{\mathrm{LOS,\,ref}} = \delta\ddot{\rho} + \delta\left(\frac{1}{\rho}\left(|\dot{\mathbf{r}}_{12}|^2 - \dot{\rho}^2\right)\right) . \tag{3}$$

To remove the dependency on measured relative velocity, Ghobadi-Far et al. (2018, 2022) designed a high-pass filter to extract the LGD from the residual range accelerations as

$$\delta g_{12}^{\mathrm{LOS,\,obs}} = \mathcal{F}^{-1}\{Z(f)\mathcal{F}\{\delta\ddot{\rho}\}\} , \tag{4}$$

with fourier inversion $\mathcal{F}$ and transfer function

$$Z(f) = \begin{cases} 1.0 & \text{for } f <= 1 \text{ mHz} \\ 1.0 + 3.5^{-4} f^{-1.04} & \text{for } 1 \text{ mHz} < f <= 0.25 \text{ Hz.} \end{cases}$$

The resulting LGD is a residual quantity that shows the difference between the observed LOS gravity and the models used in the orbit estimation (see Table 1).

2.3 Calculating line-of-sight gravity from spherical harmonic coefficients

The LGD includes not only high-frequency signals but also accumulated gravity changes. To compare this to the monthly GRACE and GRACE-FO data, we calculate the LOS gravity for a monthly and a static gravity field and take the difference. The gravitational potential is typically described using spherical harmonic coefficients (Hofmann-Wellenhof and Moritz, 2006). Taking the derivative, this potential is then expanded into the gravitational vector in spherical coordinates $\ddot{\mathbf{r}}_{r\theta\lambda}$ using SHTOOLS/pyshtools (Wieczorek et al., 2019; Wieczorek and Meschede, 2018) and rotated to cartesian coordinates as

$$\ddot{\mathbf{r}}_{xyz} = \mathbf{R}(\theta,\lambda)\ddot{\mathbf{r}}_{r\theta\lambda} = \mathbf{R}(\theta,\lambda) \begin{bmatrix} \frac{\partial V}{\partial r} \\ \frac{1}{r}\frac{\partial V}{\partial \theta} \\ \frac{1}{r\sin\theta}\frac{\partial V}{\partial \lambda} \end{bmatrix}, \tag{5}$$

with

$$\mathbf{R}(\theta,\lambda) = \begin{pmatrix} \sin\theta\cos\lambda & \cos\theta\cos\lambda & -\sin\lambda \\ \sin\theta\sin\lambda & \cos\theta\sin\lambda & \cos\lambda \\ \cos\theta & -\sin\theta & 0 \end{pmatrix} \tag{6}$$

and radius r, colatitude θ and longitude λ. The residual acceleration at position $\mathbf{x}_i$ is calculated as

$$\delta\ddot{\mathbf{r}}_i^{\text{L2}} = \ddot{\mathbf{r}}_i^{\text{L2}} - \ddot{\mathbf{r}}_i^{\text{ref}}, \tag{7}$$

where the superscript "ref" relates to the static gravity field used in the orbit estimation and "L2" is the Level 2 monthly gravity field from GRACE-FO. The LGD from Level 2 gravity field solutions $\delta g_{12}^{\text{LOS, L2}}$ is then the difference in residual acceleration projected on to the line-of-sight direction as

$$\delta g_{12}^{\text{LOS, L2}} = (\delta\ddot{\mathbf{r}}_1^{\text{L2}} - \delta\ddot{\mathbf{r}}_2^{\text{L2}}) \cdot \mathbf{e}_{12}. \tag{8}$$

The gravity fields used here are the ITSG2018 GRACE-FO monthly solutions (Mayer-Gürr et al., 2018), while the GOCO06s static field (Kvas et al., 2021) is used as the reference gravity field.

2.4 Filtering, outlier detection, and GIA correction

The LGD derived from range acceleration still contains residual high-frequency noise, and due to the limited sensitivity of the GRACE-FO system to long-wavelength signals, the low-frequency signal is degraded. To mitigate these effects, we apply

https://doi.org/10.5194/egusphere-2026-2451
Preprint. Discussion started: 8 May 2026

Butterworth filters with a cut-off frequency of $f_c = 0.001$ Hz and remove the high-frequency component from the Level 2 monthly LGD signal and the low-frequency component from the observed LGD. This separation reduces biases in the mass inversion, particularly in polar regions where Earth's flattening strongly influences the long-wavelength gravity field. The observations are now

$$\delta g_{12}^{\mathrm{LOS}} = \delta g_{12}^{\mathrm{L2,\,lf}} + \delta g_{12}^{\mathrm{obs,\,hf}} \tag{9}$$

Even after filtering, the LGD time series contains isolated outliers. We identify and remove these by comparing the observations in Eq. 9 to the smooth monthly reference signal $\delta g_{12}^{\mathrm{LOS,\,L2}}$. All samples exceeding 3σ, where σ is the standard deviation of $\delta g_{12}^{\mathrm{LOS}} - \delta g_{12}^{\mathrm{LOS,\,L2}}$, are iteratively rejected until $\sigma < 10\ \mathrm{nm\,s^{-2}}$. The final value of σ is used as the observational uncertainty in the subsequent error propagation. Long-term trends in LGD are also affected by Glacial Isostatic Adjustment (GIA), the slow viscoelastic uplift of the lithosphere following past ice-mass loss. To correct for this effect, we compute the LOS gravity contribution associated with geoid-height trends from Caron et al. (2018) and subtract it from the filtered LGD observations. The resulting corrected LGD "observations" are

$$\delta g_{12}^{\mathrm{LOS}} = \delta g_{12}^{\mathrm{L2,\,lf}} + \delta g_{12}^{\mathrm{obs,\,hf}} - \delta g_{12}^{\mathrm{GIA}}\,. \tag{10}$$

2.5 Inversion to mass change

The inversion of the LGD to mass change is based on Ghobadi-Far et al. (2022), which discusses the LGD from mass-change grids and accounts for loading effects. The change in geopotential δV_i at orbit height caused by changes in J point-masses at Earth's surface is given by the Newtonian potential

$$\delta V_i = G \sum_{j=1}^{J} \frac{\delta m_j}{d_{ij}}\,, \tag{11}$$

where d_{ij} is the distance between point-mass j and point i. Using the expansion of the inverse distance in the spectral domain (Hofmann-Wellenhof and Moritz, 2006)

$$\frac{1}{d_{ij}} = \frac{1}{R} \sum_{l=0}^{\infty} \left(\frac{R}{r}\right)^{l+1} P_l(\cos\psi_{ij})\,. \tag{12}$$

The final equation for a change in surface mass, including the change in loading on the Earth's surface, resulting in an elastic rebound of the Earth's crust, is

$$\delta V_i^{\mathrm{load}} = G \sum_{j=1}^{J} \frac{\delta m_i}{R} \sum_{l=0}^{\infty} k_l \left(\frac{R}{r}\right)^{l+1} P_l(\cos\psi_{ij})\,. \tag{13}$$

Here k_l are the load Love numbers (Farrell, 1972), and ψ_{ij} the spherical distance between the observation i on the satellite and point mass j on the Earth's surface. We use the load Love numbers for the gravitational potential k_l based on the elastic earth model PREM from Wang et al. (2012) with $k_1 = 0.026$. To reduce cut-off error, we only calculate the loading correction in the spectral domain and define the full potential as

$$\delta V_i = \delta V_i^{\mathrm{newt}} + \delta V_i^{\mathrm{load}}\,, \tag{14}$$

where δV_i^{newt} is the gravitational change related directly to the change in mass.

Similar to above, the gradient of this potential is the change in acceleration at point i due to changes in the point mass. Taking the derivative and using Eq. 6 to rotate into cartesian coordinates, the residual acceleration is calculated as

$$\delta \ddot{\mathbf{r}}^i = G \sum_{j=1}^{J} \frac{\delta m_j}{d_{ij}^3} (\mathbf{x}_i - \mathbf{x}_j) + \mathbf{R}(\theta, \lambda) \frac{G}{R^2} \begin{bmatrix} \sum_{j=1}^{J} -\delta m_j \sum_{l=0}^{\infty} k_l (l+1) \left(\frac{R}{r}\right)^{l+2} P_l(\cos\psi_{ij}) \\ \sum_{j=1}^{J} \delta m_j \sum_{l=0}^{\infty} k_l \left(\frac{R}{r}\right)^{l+2} \frac{\partial \cos\psi_{ij}}{\partial \theta} P_l'(\cos\psi_{ij}) \\ \sum_{j=1}^{J} \frac{\delta m_j}{\sin\theta} \sum_{l=0}^{\infty} k_l \left(\frac{R}{r}\right)^{l+2} \frac{\partial \cos\psi_{ij}}{\partial \lambda} P_l'(\cos\psi_{ij}) \end{bmatrix} . \tag{15}$$

The observation equation we are solving is

$$\delta g_i^{\text{LOS}} = (\delta \ddot{\mathbf{r}}_1^i - \delta \ddot{\mathbf{r}}_2^i) \cdot \mathbf{e}_{12}^i . \tag{16}$$

A simple choice for the regularisation is the Tikhonov regularisation, which we have used in earlier studies to estimate ice mass changes from monthly gravity fields (Forsberg et al., 2017; Jenny et al., 2025) and is implemented as

$$\mathbf{x} = (\mathbf{A}^T \mathbf{A} + \lambda^2 \mathbf{I})^{-1} \mathbf{A}^T \mathbf{y} , \tag{17}$$

where $\mathbf{x} = \{\delta m_j\}$ are the mass change estimates and $\mathbf{y} = \{\delta g^{\text{LOS}}\}$ are the filtered and corrected LGD and $\mathbf{I}$ is the identity matrix. This will smooth the estimated mass change, reducing noise in the resulting mass change, but it will also limit the spatial resolution. The design matrix $\mathbf{A}$ contains the partial derivative of the observation Eq. 16 w.r.t the model parameters $\mathbf{x} = \{\delta m_j\}$.

2.6 Using altimetry in regularisation matrix

To improve the spatial resolution of the mass grids from the LGD relative to the static gravity field, we incorporate altimetric height trend data $\mathbf{h}^{\text{alt}}$ from Simonsen and Sørensen (2020) into the regularisation. We construct a height-change grid using 5-year trends from the static-field reference epoch to the start of the observed month. We define a matrix $\mathbf{H}$ by setting its diagonal entries as

$$\mathbf{H}_{i,i} = \frac{\sqrt{\max|\mathbf{h}^{\text{alt}}|}}{\sqrt{|\mathbf{h}^{\text{alt}}|_{i,i}}} . \tag{18}$$

This is defined only for Greenland, given the model constraints from the CryoSat height changes. The entries for Iceland and Ellesmere Island are set to zero. These points are treated separately using a Tikhonov regularisation. This is then included in the combined GRACE-FO and CryoSat inversion to mass change as

$$\mathbf{x} = (\mathbf{A}^T \mathbf{A} + \lambda_{\text{alt}}^2 \mathbf{H}^T \mathbf{H} + \lambda_{\text{T}}^2 \mathbf{I}_{\text{I,E}})^{-1} \mathbf{A}^T \mathbf{y} , \tag{19}$$

where $\mathbf{I}_{\text{I,E}}$ is one for the diagonal entries corresponding to the mass points in Iceland and the Ellesmere Island and zero otherwise, $\mathbf{x} = \{\delta m_j\}$, $\mathbf{y} = \{\delta g^{\text{LOS}}\}$ and $\mathbf{A}$ are defined as in Eq. 17.

L-curve

For both choices of regularisation, we use the L-curve criterion to select the regularisation parameters λ or λ_{alt} and λ_{T}. The misfit norm $(\mathbf{Ax}-\mathbf{y})^T(\mathbf{Ax}-\mathbf{y})$ is a measure for how much the modelled LGD describes the observed LGD. The model norm $\mathbf{x}^T\mathbf{H}^T\mathbf{Hx}$ is a measure for the total mass change scaled with the regularisation matrix. The "knee" of the L-curve is the point where the model norm increases while the misfit norm does not improve further. This is the point at which the ratio of noise to residuals is optimised. Figure 2 shows this for the choice of λ_{alt} and λ_{T} in the case of the altimetry-based regularisation, and Fig. 3 shows it for the simpler case of only Tikhonov regularisation. These plots show that both the total mass estimate and the residuals plateau for small regularisation parameters. The L-curves for both regularisation schemes do not show a clear "best" choice. We looked at all 59 sets of 5 days and chose one set of regularisation based on these sets of plots. This is, to some extent, a subjective choice, and we chose to go with a slightly lower regularisation than the L-curve would suggest to include most of the signal. This process would have to be repeated if the observation periods are changed to account for the change in spatial coverage of the data.

3 Results and discussion

We show below the results of inverting 5-day data windows for four summers. We compare the results for the entire Greenland to other solutions, and we examine the Ilulissat glacier to assess whether we can resolve this smaller area and how the altimetry-based regularisation affects the spatial distribution of the estimated mass change.

3.1 Greenland mass balance

Figure 4 shows the estimated mass change since the reference epoch for the two different regularisation schemes. They also show the conventional CCI solution by Barletta et al. (2020) (green) and the GravIS solution by Sasgen et al. (2020) (brown) for comparison. To compare the submonthly signal, we also included the daily Greenland Mass Balance (GMB) in grey by Barletta et al. (2024), which is based on 58 stations of the GNSS Network GNET. This dataset is based on the proportional relationship between each station's uplift and nearby mass changes. We restored the trend of -231.48 Gt/yr. The estimated mass change based on the LGD generally agrees with the two monthly solutions, CCI (green) and GravIS (brown), as these two solutions also show an offset when calculating the mass change from the time series since 2010-01-01. As expected, the mass change estimates from 5 days of LGD data are less smooth than those based on the monthly gravity fields. Both regularisation schemes yield comparable solutions, providing confidence that the chosen regularisation does not affect the total mass change when the regularisation parameters are appropriately chosen. The LGD solutions generally follow the independent daily GNET GMB quite well. The error bars of the LGD inversion are solely based on the covariance matrix and the standard deviation after fitting. The full covariance matrix is calculated as

$$\mathrm{Cov}(\mathbf{x}) = \sigma^2_{\text{obs}}\mathbf{N}^{-1}\mathbf{A}^T\mathbf{A}\mathbf{N}^{-1}$$

https://doi.org/10.5194/egusphere-2026-2451
Preprint. Discussion started: 8 May 2026

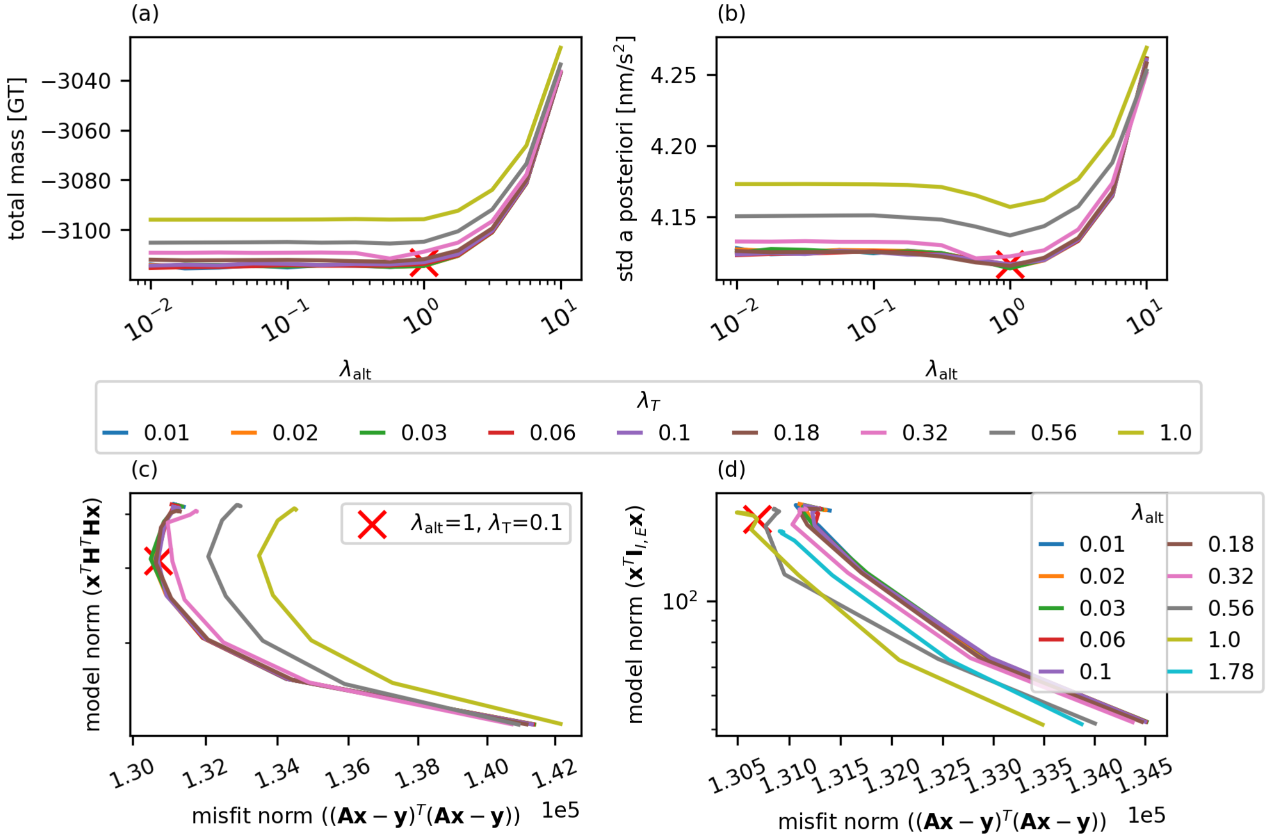

Figure 2. This figure shows (a) total mass change in Gt and (b) standard deviation of the residuals after the inversion for different choices of regularisation parameters for the case where altimetry data were used to set up the regularisation matrix. The L-curves are shown in (c) in λ_{alt} for the different choices of $\lambda_{\mathrm{I,E}}$ and in (d) in $\lambda_{\mathrm{I,E}}$ for the different choices of λ_{alt}. This figure shows the results of a single set of observations, randomly selected from the 59 sets. Note that the model norm only includes the relevant regularisation matrix. The x-axes are on a logarithmic scale, but the misfit norm varies only over a limited interval within this logarithmic domain. The chosen regularisation is marked with an x.

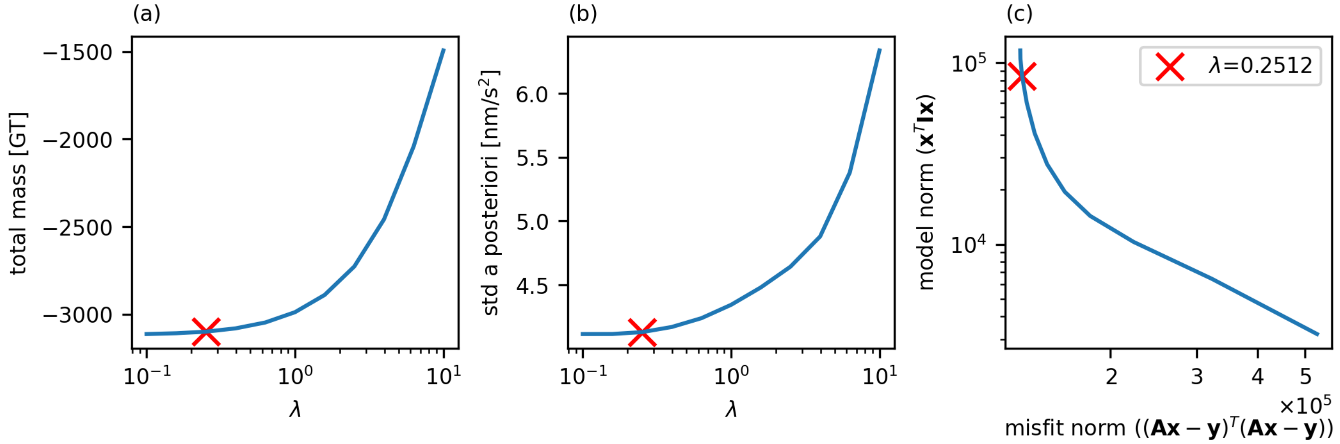

Figure 3. This figure shows (a) total mass change in Gt and (b) standard deviation of the residuals after the inversion for different choices of regularisation parameters. The L-curve is shown in (c). This figure shows the results for the same set of observations as Fig. 2. The x-axes are on a logarithmic scale, but the misfit norm varies only over a limited interval within this logarithmic domain. The chosen regularisation is marked with an x.

where $\mathbf{N} = \mathbf{A}^T\mathbf{A} + \lambda^2\mathbf{I}$ or $\mathbf{N} = \mathbf{A}^T\mathbf{A} + \lambda_{\text{alt}}^2\mathbf{H}^T\mathbf{H} + \lambda_{\text{T}}^2\mathbf{I}_{\text{I,E}}$ respectively. The mass estimates from the altimetry regularisation are highly correlated, resulting in larger error estimates.

Table 2 shows the standard deviation of the residuals of the observations with respect to the LGD of the monthly gravity field and to the modelled LGD in nm/s^2 for all four years. The observations show decreasing standard deviations of the residuals over the years for both LGD from monthly fields and modelled point masses. We have not investigated the source of the decrease in observation noise. One possible reason is improved orbit estimation resulting from improved accelerometer transplant for the second satellite in the GRACE-FO pair, GRACE-D. Table 2 also shows that the standard deviation of the residuals from both inversion regularisations is consistently higher than that of the residuals based on the monthly gravity field. The reason for these higher residuals in the point-mass inversions is not investigated. Since the inversion seems to perform worse than the monthly gravity field solution as noise decreases, we suspect that we are hitting the natural limit imposed by the limited spatial distribution of the observations. While the monthly solution uses all available data, we have at most 5 days of data, each with 2 to 6 orbits crossing our observation area.

Table 2. Standard deviations of the residuals for LGD from the monthly field and the two different regularisations.

	2019	2020	2021	2022
σ_{monthly}	5.11 nm/s^2	4.04 nm/s^2	2.90 nm/s^2	2.78 nm/s^2
$\sigma^{\text{altimetry}}$	5.12 nm/s^2	4.09 nm/s^2	3.41 nm/s^2	3.28 nm/s^2
σ^{Tikhonov}	5.13 nm/s^2	4.12 nm/s^2	3.45 nm/s^2	3.30 nm/s^2

Figure 5 shows the mass change split up into the Zwally basins (Zwally et al., 2012). The centre figure (a) is the gridded mass

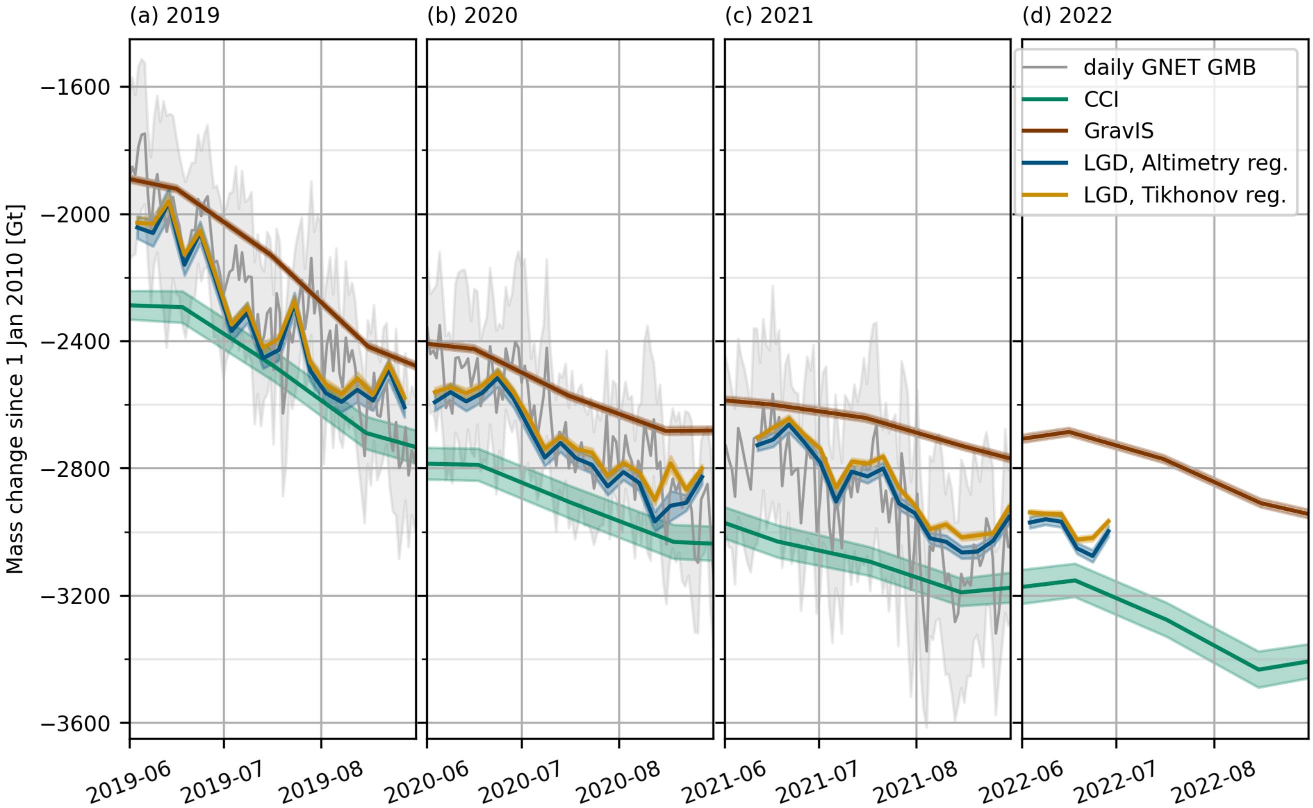

Figure 4. (a)–(d) show the total Greenland Mass Change (GMB) since 2010-01-01 for the two different regularisation schemes. We show the 5-day solutions for the summer periods 2019 to 2022. For comparison, the GravIS and DTU Space CCI solutions are also plotted. In grey, we show the daily GMB based on the data of 58 stations of the GNSS Network GNET.

change for the end of the observation period (2022-06-26 to 2022-06-30) using the altimetry regularisation, and the line plots (b–i) show the CCI result compared to our LGD inversion for all eight basins. The basins are numbered clockwise, starting at the top, and the black lines in (a) show the basin outlines. The basins are also shown in Fig. 1 for reference. While the results for basins 2, 3 and 5 agree very well with the CCI solution, the mass change is smaller for all basins compared to the CCI solution. This agrees with the results for the whole Greenland Ice Sheet (GrIS) in Fig. 4, where the solutions based on LGD estimate a lower mass loss than the reference time series by Barletta et al. (2020). Comparing the centre figure (a) to the height trends in Fig. 1 shows the fingerprint of the altimetry data in the resulting mass change. The mass gain areas are mostly at the inland borders of the basins, which is expected. The basins 6 (g) and 8 (i) show increased mass loss in summer 2019. Comparing basins 4 and 6 shows that the spatial distribution of the mass change depends on the regularisation, as basin 4 shows higher mass loss for the altimetry regularisation, but basin 6, which shares a border with basin 4, shows higher mass

https://doi.org/10.5194/egusphere-2026-2451
Preprint. Discussion started: 8 May 2026

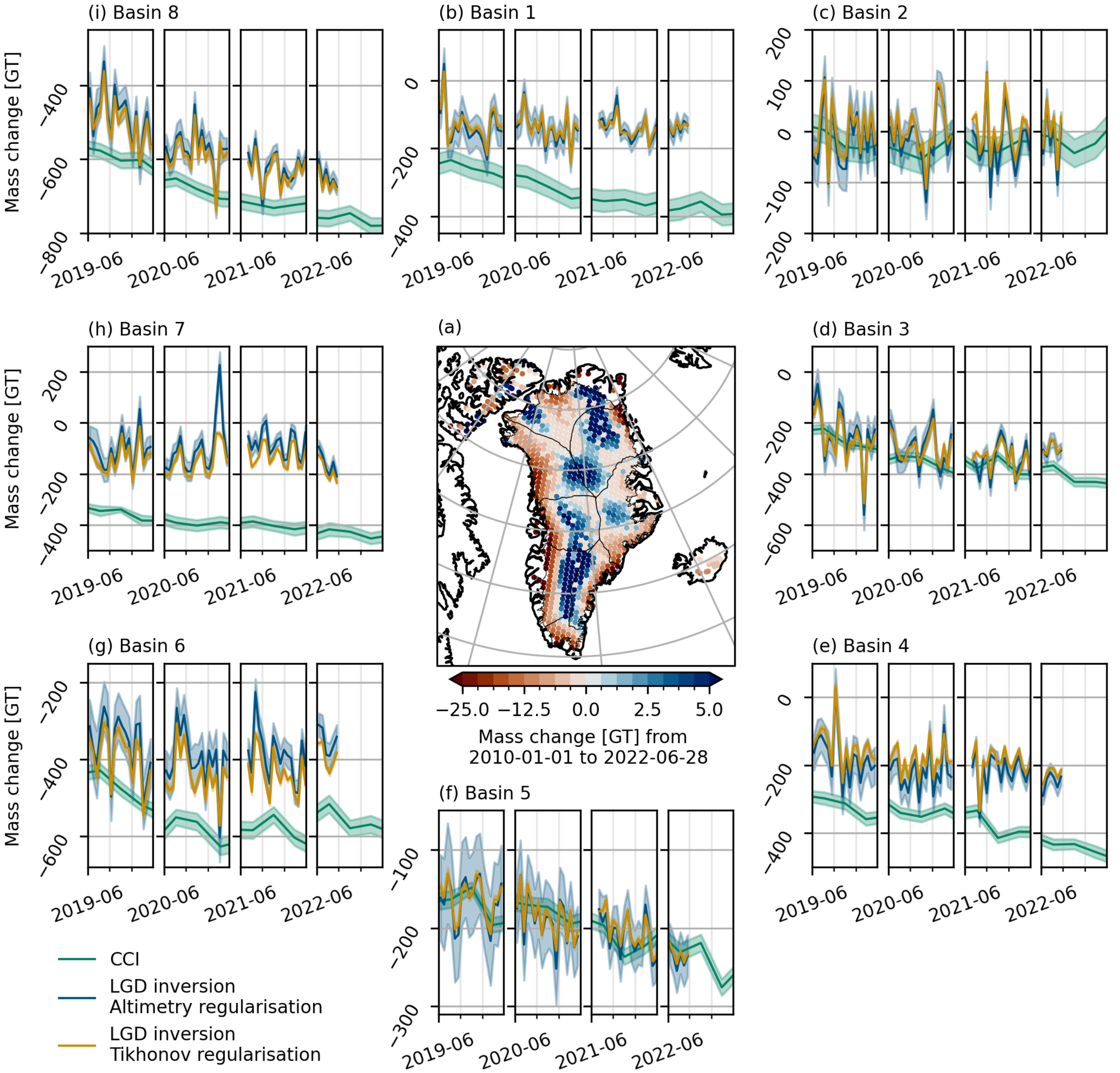

Figure 5. Mass Change since 2010 for the eight Zwally basins compared to the DTU Space CCI solutions. Note the asymmetric colour bar in (a), and the different scales of the y-axis and broken x-axis in (b)–(i).

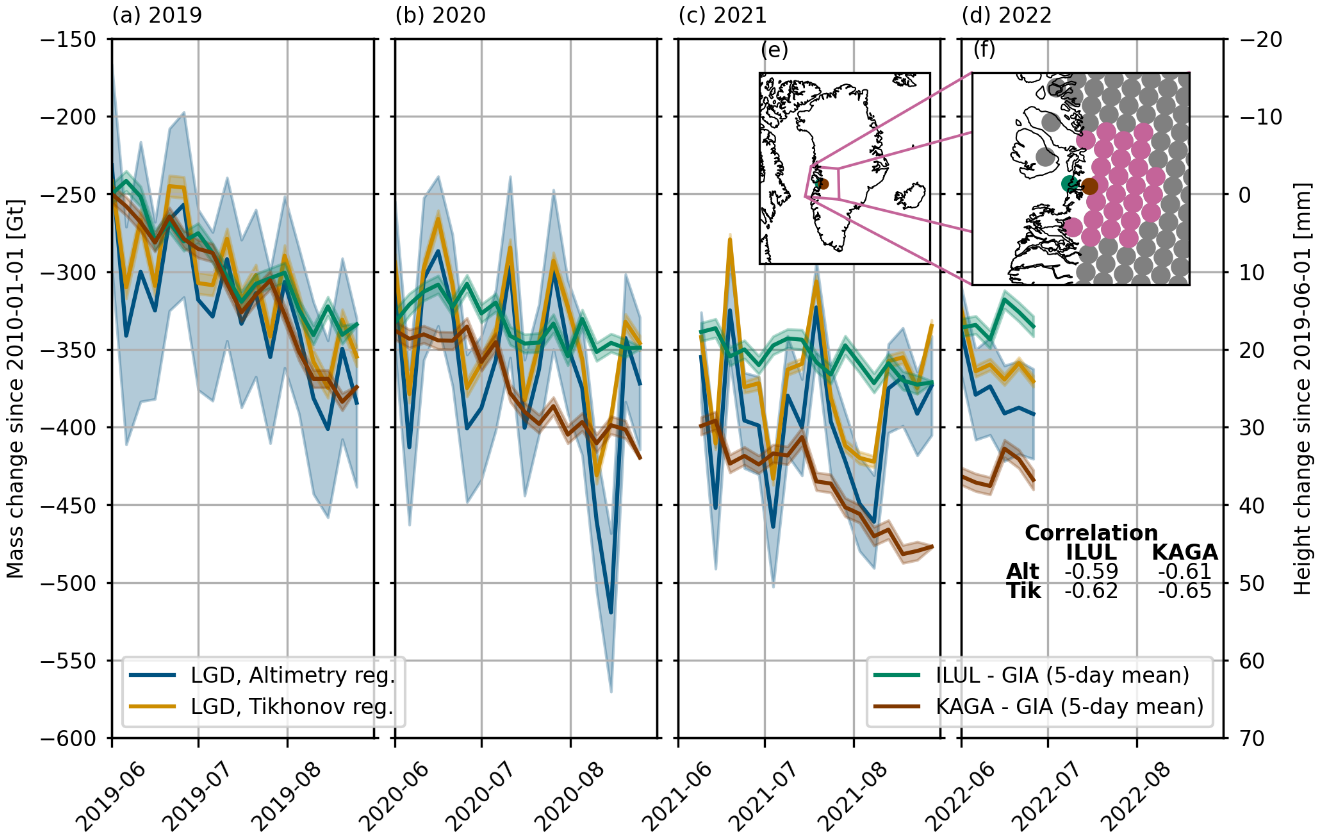

	ILUL	KAGA
Alt	-0.59	-0.61
Tik	-0.62	-0.65

Figure 6. (a) – (d) Mass change since 2010-01-01 for the Ilulissat region (left y-axis) and vertical displacement of two GNET stations ILUL and KAGA minus the GIA trend (right y-axis). The relative scale between the two units is arbitrary, but the correlation between uplift and mass change is shown in the bottom right. (e) and (f) show the Ilulissat region in pink and the location of the two GNET stations.

loss for the Tikhonov regularisation.

3.2 Ilulissat area mass balance

Figure 6 shows the mass change time series from the LGD inversion for the region around the Ilulissat glacier, the biggest outlet glacier in Greenland. The chosen mascon points are marked in pink, and the lines show the sum over these points for all 5-day sets. This area lies at the boundary of basins 6 and 7.

This figure shows a mass loss of about 100 Gt in the summer of 2019 and about 50 Gt or less in the summers of 2020 and 2021. While the two solutions generally agree on the trends, the mass change based on the altimetry regularisation estimates a slightly larger change since 2010-01-01. For comparison, we include the vertical displacement measured at two GNET stations

https://doi.org/10.5194/egusphere-2026-2451
Preprint. Discussion started: 8 May 2026

in the area (Solgaard et al., 2026), with the GIA signal removed (Berg et al., 2023). To make them more comparable to our solutions, we took the 5-day mean. Both stations show increased uplift during summer 2019 and partially also in 2020 and 2021. For the whole time series, the correlation between the GNET uplift data and the LGD mass change estimates is between -0.59 and -0.65. The KAGA station, which is closer to the glacier, shows a slightly higher correlation. Interestingly, the Tikhonov regularisation also shows a slightly higher correlation with the uplift data.

3.3 Overall discussion

The results presented above show that line-of-sight gravity differences (LGD) can be used to calculate sub-monthly mass-change grids for Greenland. The results for mass change for the total GrIS compare well with the monthly mass change solutions by Barletta et al. (2020) and Sasgen et al. (2020) and fit quite well with the daily GNET GMB by Barletta et al. (2024), giving us confidence that both methods, LGD and GNET, observe real sub-monthly mass change signals. Both Tikhonov and Altimetry regularisation show similar mass change for the total GrIS, but the difference in spatial distribution is reflected in the basin time series, and when looking at more local features, such as the region around Ilulissat. To investigate which regularisation best fits the actual distribution of mass change, other GNET stations and different LGD spatial resolutions also need to be evaluated.

Since we use the monthly gravity field solutions to filter the low-frequency signal in the LGD data, we are not completely independent of them. While the regularisation drives the spatial distribution, the results for the area around Ilulissat agree well with each other at the beginning of the observation period. The point-mass mascon approach is well established and would be a candidate processing scheme for future missions such as ESA's NGGM. We are only using the LRI data in this study, but the KBR data could be used to improve data coverage and extend the time series, albeit with lower accuracy.

The altimetry regularisation is based on surface elevation changes by Simonsen and Sørensen (2020), which is only available for the GrIS. To improve the spatial distribution of mass changes, also for Iceland and Ellesmere Island, other altimetry products (IceSat-2) or a regularisation based on velocity maps could be considered. For future work, a focused study on Iceland could be considered, in which the method is adapted for more regional applications while ensuring that the signal from Greenland is removed from the LGD before inversion, see Sørensen et al. (2017).

4 Conclusions

We have shown that inverting line-of-sight gravity differences (LGD) to weekly mass change yields reasonable results for ice mass changes in Greenland during summers 2019 to 2022. We introduced both a Tikhonov regularisation and a regularisation based on surface-height trends from altimetry. We found that the two schemes agree well over the entire Greenland Ice Sheet (GrIS) but exhibit different spatial distributions at the basin scale or in more regional features. This method is interesting because it directly inverts LGD into ground mass change, which could be extended to data assimilation in ice sheet models, similar to Khaki et al. (2023). This method, combined with monthly gravity field solutions for the long-wavelength signal, is a promising approach for estimating the gravity field and mass change at regional scales.

Code and data availability. The data and code supporting the findings of this study are currently being prepared for public release. In the meantime, they are available from the corresponding author upon request.

Author contributions. All authors contributed to the definition of the research aims and to extending the method. BJ implemented the method, performed the data analysis, prepared the plots and wrote the manuscript draft. All authors reviewed and edited the manuscript.

Competing interests. The authors declare that they have no conflict of interest.

Acknowledgements. The authors would like to thank Shin-Chan Han for his support and code snippets during the initial phase of the project. We also want to thank Valentina Barletta, Sebastian Simonsen, Louise Sørensen and the whole team at the GEO Department at DTU Space for all their input at various discussions. In preparing this article, we used AI-assisted tools, Microsoft 365 Copilot (Microsoft, 2026), and Grammarly Pro (Inc., 2026), for tasks such as language editing, text refinement, and clarity improvement. We also used AI tools to assist in generating and refining Python scripts for data processing and plotting, with all code subsequently reviewed, tested, and adapted by BJ. This work was partly supported by the EU project CARIOQA-PMP.

References

Barletta, V. R., Sørensen, L. S., Simonsen, S. B., and Forsberg, R.: Gravitational mass balance of Greenland 2003 to present v3.0, Dataset, Technical University of Denmark, https://doi.org/10.11583/DTU.12866579.v5, 2020.

Barletta, V. R., Bordoni, A., and Khan, S. A.: GNET Derived Mass Balance and Glacial Isostatic Adjustment Constraints for Greenland, Geophysical Research Letters, 51, e2023GL106 891, https://doi.org/https://doi.org/10.1029/2023GL106891, e2023GL106891 2023GL106891, 2024.

Berg, D. L., Barletta, V., Hassen, J., et al.: Vertical land motion due to present-day ice loss from Greenland's and Canada's peripheral glaciers, https://doi.org/10.5061/dryad.9zw3r22n0, dataset, 2023.

Caron, L., Ivins, E. R., Larour, E., Adhikari, S., Nilsson, J., and Blewitt, G.: GIA Model Statistics for GRACE Hydrology, Cryosphere, and Ocean Science, Geophysical Research Letters, 45, 2203–2212, https://doi.org/https://doi.org/10.1002/2017GL076644, 2018.

Desai, S. D.: Observing the pole tide with satellite altimetry, Journal of Geophysical Research: Oceans, 107, 7–1, https://doi.org/10.1029/2001jc001224, 2002.

Farrell, W. E.: Deformation of the Earth by surface loads, Reviews of Geophysics, 10, 761–797, https://doi.org/10.1029/RG010I003P00761;JOURNAL:JOURNAL:19449208;CTYPE:STRING:JOURNAL, 1972.

Folkner, W. M., Williams, J. G., Boggs, D. H., Park, R. S., and Kuchynka, P.: The Planetary and Lunar Ephemerides DE430 and DE431, 2014.

Forsberg, R., Sørensen, L. S., and Simonsen, S.: Greenland and Antarctica Ice Sheet Mass Changes and Effects on Global Sea Level, 38, 91–106, https://doi.org/10.1007/978-3-319-56490-6_5, 2017.

Gérard, P. and Luzum, B.: IERS Conventions (2010), Bureau International Des Poids Et Mesures Sevres (France), pp. 1–179, http://www.iers.org/TN36/, 2010.

Ghobadi-Far, K., Han, S. C., Weller, S., Loomis, B. D., Luthcke, S. B., Mayer-Gürr, T., and Behzadpour, S.: A Transfer Function Between Line-of-Sight Gravity Difference and GRACE Intersatellite Ranging Data and an Application to Hydrological Surface Mass Variation, Journal of Geophysical Research: Solid Earth, 123, 9186–9201, https://doi.org/10.1029/2018JB016088;SUBPAGE:STRING:FULL, 2018.

Ghobadi-Far, K., Han, S. C., McCullough, C. M., Wiese, D. N., Ray, R. D., Sauber, J., Shihora, L., and Dobslaw, H.: Along-Orbit Analysis of GRACE Follow-On Inter-Satellite Laser Ranging Measurements for Sub-Monthly Surface Mass Variations, Journal of Geophysical Research: Solid Earth, 127, e2021JB022 983, https://doi.org/10.1029/2021JB022983;WGROUP:STRING:PUBLICATION, 2022.

Hofmann-Wellenhof, B. and Moritz, H.: Physical geodesy (Second, corrected edition), Physical Geodesy (Second, corrected edition), pp. 1–403, https://doi.org/10.1007/978-3-211-33545-1/COVER, 2006.

Inc., G.: Grammarly, https://www.grammarly.com, accessed: 2026-04-28, 2026.

Ince, E. S., Barthelmes, F., Reißland, S., Elger, K., Förste, C., Flechtner, F., and Schuh, H.: ICGEM – 15 years of successful collection and distribution of global gravitational models, associated services, and future plans, Earth System Science Data, 11, 647–674, https://doi.org/10.5194/essd-11-647-2019, 2019.

Jenny, B., Jensen, T. E., and Forsberg, R.: Mass Change in Antarctica from 2002 to 2025 Using GRACE and GRACE-FO, Remote Sensing 2025, Vol. 17, Page 3870, 17, 3870, https://doi.org/10.3390/rs17233870, 2025.

Khaki, M., Han, S.-C., Ghobadi-Far, K., Yeo, I.-Y., and Tangdamrongsub, N.: Assimilation of GRACE Follow-On Inter-Satellite Laser Ranging Measurements Into Land Surface Models, Water Resources Research, 59, e2022WR032 432, https://doi.org/https://doi.org/10.1029/2022WR032432, e2022WR032432 2022WR032432, 2023.

Kurtenbach, E., Eicker, A., Mayer-Gürr, T., Holschneider, M., Hayn, M., Fuhrmann, M., and Kusche, J.: Improved daily GRACE gravity field solutions using a Kalman smoother, Journal of Geodynamics, 59-60, 39–48, https://doi.org/10.1016/J.JOG.2012.02.006, 2012.

Kvas, A., Behzadpour, S., Ellmer, M., Klinger, B., Strasser, S., Zehentner, N., and Mayer-Gürr, T.: ITSG-Grace2018: Overview and evaluation of a new GRACE-only gravity field time series, Journal of Geophysical Research: Solid Earth, 124, 9332–9344, https://doi.org/10.1029/2019JB017415, 2019.

Kvas, A., Brockmann, J. M., Krauss, S., Schubert, T., Gruber, T., Meyer, U., Mayer-Gürr, T., Schuh, W. D., Jäggi, A., and Pail, R.: GOCO06s-A satellite-only global gravity field model, Earth System Science Data, 13, 99–118, https://doi.org/10.5194/essd-13-99-2021, 2021.

Landerer, F. W., Flechtner, F., Save, H., and Dahle, C.: GRACE Follow-On Science Data System Newsletter No. 24: Apr–Jul 2023, Science Data System Newsletter No. 24, GRACE-FO Science Data System, Jet Propulsion Laboratory / California Institute of Technology, GFZ German Research Centre for Geosciences, Center for Space Research at the University of Texas at Austin, https://isdc-data.gfz.de/grace-fo/DOCUMENTS/NEWSLETTER/2023/GRACE-FO_SDS_NL_024_202304.pdf, period: Apr–Jul 2023, 2023.

Li, H.-S., Yi, S., ren Luo, Z., and Xu, P.: Revealing High-Temporal-Resolution Flood Evolution With Low Latency Using GRACE Follow-On Ranging Data, Water Resources Research, 60, e2023WR036 332, https://doi.org/10.1029/2023WR036332, 2024.

Li, H.-s., Yi, S., Han, S.-C., and Tang, H.: Daily Regional Gravity Field Estimation Using GRACE Follow-On Line-of-Sight Gravity Differences, Journal of Geophysical Research: Solid Earth, 130, e2024JB030 089, 2025.

Lyard, F. H., Allain, D. J., Cancet, M., Carrère, L., and Picot, N.: FES2014 global ocean tide atlas: Design and performance, Ocean Science, 17, 615–649, https://doi.org/10.5194/os-17-615-2021, 2021.

Mayer-Gürr, T., Behzadpour, S., Eicker, A., Ellmer, M., Koch, B., Krauss, S., Pock, C., Rieser, D., Strasser, S., Süsser-Rechberger, B., Zehentner, N., and Kvas, A.: GROOPS: A software toolkit for gravity field recovery and GNSS processing, Computers & Geosciences, 155, 104 864, https://doi.org/10.1016/j.cageo.2021.104864, 2021.

Mayer-Gürr, T., Behzadpour, S., Ellmer, M., Kvas, A., Klinger, B., Strasser, S., and Zehentner, N.: ITSG-Grace2018 – Monthly, Daily and Static Gravity Field Solutions from GRACE, Dataset, GFZ Data Services: Potsdam, Germany, https://doi.org/10.5880/ICGEM.2018.003, 2018.

Microsoft: Microsoft Copilot, https://copilot.microsoft.com, accessed: 2026-04-28, 2026.

NASA Jet Propulsion Laboratory (JPL): GRACE-FO Level-1B Release version 4.0 from JPL in ASCII, NASA Physical Oceanography Distributed Active Archive Center, https://doi.org/10.5067/GFL1B-ASJ04, 2019.

Sasgen, I., Groh, A., and Horwath, M.: COST-G GravIS RL01 Ice-Mass Change Products, Dataset, https://doi.org/10.5880/COST-G.GRAVIS_01_L3_ICE, 2020.

Shihora, L., Balidakis, K., Dill, R., Dahle, C., Ghobadi-Far, K., Bonin, J., and Dobslaw, H.: Non-Tidal Background Modeling for Satellite Gravimetry Based on Operational ECWMF and ERA5 Reanalysis Data: AOD1B RL07, Journal of Geophysical Research: Solid Earth, 127, e2022JB024 360, https://doi.org/10.1029/2022JB024360, 2022.

Simonsen, S. B. and Sørensen, L. S.: Greenland Surface elevation change 1992 to present (2024 release), Dataset, Technical University of Denmark, https://doi.org/10.11583/DTU.12866000.v4, 2020.

Solgaard, C., Winther-Dahl, M. N., Nylen, T., Madsen, F. B., Hansen, O. B., Berg, D. L., Hassan, J., Knudsen, P., Bevis, M., and Khan, S. A.: Daily coordinate time series from the Greenland GNSS Network (GNET) from 1995 - 2025., https://doi.org/10.11583/DTU.31397901.v1, 2026.

Sulzbach, R., Balidakis, K., Dobslaw, H., and Thomas, M.: TiME22: Periodic Disturbances of the Terrestrial Gravity Potential Induced by Oceanic and Atmospheric Tides, https://doi.org/https://doi.org/10.5880/nerograv.2022.006, 2022.

Sørensen, L. S., Jarosch, A. H., Adalgeirsdóttir, G., Barletta, V. R., Forsberg, R., Pálsson, F., Björnsson, H., and Jóhannesson, T.: The effect of signal leakage and glacial isostatic rebound on GRACE-derived ice mass changes in Iceland, Geophysical Journal International, 209, 226–233, https://doi.org/10.1093/GJI/GGX008, 2017.

Wang, H., Xiang, L., Jia, L., Jiang, L., Wang, Z., Hu, B., and Gao, P.: Load Love numbers and Green's functions for elastic Earth models PREM, iasp91, ak135, and modified models with refined crustal structure from Crust 2.0, Computers & Geosciences, 49, 190–199, https://doi.org/10.1016/j.cageo.2012.06.022, 2012.

Wieczorek, M., Meschede, M., de Andrade, E. S., Oshchepkov, I., Xu, B., and Walker, A.: SHTOOLS: Version 4.5, Zenodo, https://doi.org/10.5281/ZENODO.3457861, 2019.

Wieczorek, M. A. and Meschede, M.: SHTools: Tools for Working with Spherical Harmonics, Geochemistry, Geophysics, Geosystems, 19, 2574–2592, https://doi.org/10.1029/2018GC007529, 2018.

Zwally, H. J., Giovinetto, M. B., Beckley, M. A., and Saba, J. L.: Antarctic and Greenland drainage systems, GSFC Cryospheric Sciences Laboratory, https://earth.gsfc.nasa.gov/cryo/data/polar-altimetry/antarctic-and-greenland-drainage-systems, 2012.